International Journal of analytical and Numerical Methods in Mechanical Design
Vol 2., Issue 2, Summer & Autumn 2023, 7-18

The method of numerical analysis of the behavior of drained sands in monotonic loading

Farzad Peyman[a, *]

[a, *]Faculty of Civil Engineering, Islamic Azad University, Qazvin Branch, Qazvin, Iran

Received 05 September 2023, Accepted 21 November 2023

Abstract

The primary purpose of studying the behavior of sand is to calculate its deformation at loading. The granular structure of the sand causes the transfer of forces through multiple contacts of the particles. Its deformation results from the combination of slip and roll of the particles. Accordingly, changes in the sand modulus matrix are observed and considered in this research. The studies show that by assuming different spring behavior in each loading increment for the set of sand particles, a numerical linear-nonlinear behavior can be defined according to the drained experimental results. Therefore, proportional numerical functions are defined based on the trend of changes in the modulus of elasticity and changes in the Poisson ratio of sand during monotonic loading. The coefficients are obtained from the related experimental results. The computational effects of these functions in the analytical method are used to convert the experimental behavior of sand into a numerical behavior. The validity of this numerical method is based on calibration and comparison with valid experimental results. In addition to hardening behavior, this numerical analysis can define softening behavior.

Keywords: sand, modulus matrix, damage, drained, monotonic loading, numerical method, softening

1. Introduction

Sand is obtained from the deposition of equilibrium particles of quartz, feldspar, and other minerals, with a size of about 0.06 to 2 mm. The intergranular forces are transmitted through contact and interaction. For this reason, sands show complex behavior in different environmental conditions and loads.

When shear stress is applied to sand, the deformation created is accompanied by a change in volume, resulting from a combination of two competitive states of accumulated displacement of its particles, namely slipping and rolling. Sliding displacement of particles through the accumulation of sand particles indicates a tendency to reduce the volume to reach a more stable state. However, the rolling mechanism, characteristic of dense sand behavior, tends to increase in volume. When slipping occurs, the particles fill the pore space between them as much as possible but do not move much in the direction of the cutting path. Therefore, sliding displacement can quickly occur without developing a large amount of shear strain. This is why the reduction in volume on loose sand is seen with a large reduction in relative density in the early stages of loading.

On the other hand, creating a larger displacement requires adjacent rolling particles on top of each other. This is why an increase in volume or dilation occurs in the later stages of shear stress, in which the sand is significantly deformed. These two mechanisms usually work together and are seen in the stress-strain behavior of laboratory specimens. In this way, sands in different environmental conditions and loads have complex behavior that can attract researchers' attention [1-2].

*Corresponding author Email address: f.peyman@srbiau.ac.ir

Many analytical models have been proposed to define and predict the behavior of sand. However, some of them cannot express all the properties and characteristics of behavior, and others are so difficult that their use in practical cases is costly and eliminated. Studies show that recent models can be divided into continuous and discontinuous groups. In continuous models, it is assumed that the material operates seamlessly and there is no discontinuity, including cracking, slipping, separation or failure. In discontinuous models, the material is thought of as a set of particles that can affect each other's motion.

Continuous models into two subgroups: macro, based on theories of paste or damage or a combination of both [3-9], and are divided into mesoscopic, such as micro-plane or multi-laminate models [10-13]. Discontinuous models also lead to a subset called micro models, such as discrete particle models [14-16].

In macro models, material behavior is defined based on the direct relationship between stress and strain tensors [17-24]. However, in mesoscopic models, the material's behavior is clearly defined by the relationship between stress and strain vectors on planes, known as micro-plane or multi-laminate planes [25-31]. In discontinuous models, the material's behavior is simulated based on the definition of interparticle forces due to their motion on each other and their use in the equation of motion and numerical solution. In discontinuous models, the material's behavior is simulated by numerical solution based on the definition of interparticle forces due to their motion relative to each other and the use of motion equation [32-33].

In this comparison, discontinuous models define the behavior of materials better than other models due to the precise and close-to-reality type of payment. However,

using them can be difficult, complicated, and costly for engineering purposes. On the other hand, macro models based on stress or strain invariants cannot simulate the behavioral properties of direction-dependent materials. These models make it impossible to store information dependent on different directions. Therefore, mesoscopic models are a logical and intermediate solution between the two groups. For these reasons, in the present research, a method based on damage theory has been developed that can be used in multi-laminate models for numerical analysis of drained sands behavior at monotonic loading [34].

2. Numerical analysis of drained sand behavior based on modulus matrix changes

The main purpose of studying soils under different environmental conditions and loads is to calculate their deformation. In this connection, the particle structure of the sands causes the forces to be transmitted through multiple contacts of the particles, and their deformation results from the effects of slipping and rolling of the particles. Accordingly, changes in the modulus matrix of the drained sands in different void ratios and relative densities are observed at monotonic loading. A suitable numerical analysis method can be presented to define the nonlinear behavior of saturated sands in these conditions. The calibration of the latter method is obtained from related experimental results such as triaxial compression testing.

2.1. Module matrix changes

In this method, based on the principal stress space in monotonic loading tests, in each load increase increment, the behavior of saturated sand can be considered homogeneous, isotropic, linear elasticity, and, of course, different from the previous and next load increment. In other words, the perspective of hypo-elastic behavior was considered a criterion. Depending on the type of experiment, the general form of damage and change functions in numerical analysis was proposed. To begin with, in each loading increment i, the relationship between the stress and strain vectors in the principal stress space can be represented as Equation (1).

$$\begin{Bmatrix}\sigma_{1i}\\ \sigma_{2i}\\ \sigma_{3i}\end{Bmatrix}=\frac{E_i}{(1+\nu_i)(1-2\nu_i)}\begin{bmatrix}1-\nu_i & \nu_i & \nu_i\\ \nu_i & 1-\nu_i & \nu_i\\ \nu_i & \nu_i & 1-\nu_i\end{bmatrix}\begin{Bmatrix}\varepsilon_{1i}\\ \varepsilon_{2i}\\ \varepsilon_{3i}\end{Bmatrix} \quad (1)$$

For a cylindrical sample in a triaxial compression test, Equation (1) is rewritten as (2) at the deviator stress increment stage.

$$\begin{Bmatrix}\sigma_{1i}\\ \sigma_{3i}\\ \sigma_{3i}\end{Bmatrix}=\begin{Bmatrix}\sigma_3\\ \sigma_3\\ \sigma_3\end{Bmatrix}+\begin{Bmatrix}\Delta\sigma_i\\ 0\\ 0\end{Bmatrix}=\begin{Bmatrix}\sigma_3\\ \sigma_3\\ \sigma_3\end{Bmatrix}+$$

$$\frac{E_i}{(1+\nu_i)(1-2\nu_i)}\begin{bmatrix}1-\nu_i & \nu_i & \nu_i\\ \nu_i & 1-\nu_i & \nu_i\\ \nu_i & \nu_i & 1-\nu_i\end{bmatrix}\begin{Bmatrix}\varepsilon_{1i}\\ \varepsilon_{3i}\\ \varepsilon_{3i}\end{Bmatrix} \quad (2)$$

From the expansion of Equation (2), Equations (3) and (4) are obtained.

$$\sigma_{1i}=\sigma_3+\frac{E_i}{(1+\nu_i)(1-2\nu_i)}\cdot[(1-\nu_i)\varepsilon_{1i}+2\nu_i\varepsilon_{3i}] \quad (3)$$

$$\sigma_{3i}=\sigma_3+\frac{E_i}{(1+\nu_i)(1-2\nu_i)}\cdot(\nu_i\varepsilon_{1i}+\varepsilon_{3i}) \quad (4)$$

In which:

$$\nu_i=-\frac{\varepsilon_{3i}}{\varepsilon_{1i}} \quad (5)$$

In these equations and each loading increment *i*:

σ_{3i}= Minor principal stress in every increment
σ_{2i}= Middle principal stress in every increment
σ_{1i}= Major principal stress in every increment
ε_{3i}= Minor principal strain in every increment
ε_{2i}= Middle principal strain in every increment
ε_{1i}= Major principal strain in every increment
σ_3= Minor principal stress
E_i= Modulus of elasticity in every increment
ν_i= Poisson ratio in every increment

Equation (5) in Equation (4) will lead to the reality of Equation (6).

$$\sigma_{3i}=\sigma_3+\frac{E_i}{(1+\nu_i)(1-2\nu_i)}\cdot(-\varepsilon_{3i}+\varepsilon_{3i})=\sigma_3+0=\sigma_3 \quad (6)$$

In the following, parameters such as mean and shear stresses and volumetric strain in each loading increment are defined as Equations (7) to (9).

$$p_i=\frac{\sigma_{1i}+2\sigma_{3i}}{3}=\frac{\sigma_{1i}+2\sigma_3}{3} \quad (7)$$

$$q_i=\sigma_{1i}-\sigma_{3i}=\sigma_{1i}-\sigma_3=\Delta\sigma_i \quad (8)$$

$$\varepsilon_{vi}=\varepsilon_{1i}+2\varepsilon_{3i}=(1-2\nu_i)\cdot\varepsilon_{1i} \quad (9)$$

In which:

q_i= Deviatoric stress in every increment
p_i= Mean stress in every increment
ε_{vi}= Volumetric strain in every increment

From the placement of Equation (3) in Equations (7) and (8) and the use of Equations (9) and (5) in them, we can conclude Equations (10) and (11).

$$p_i=\frac{q_i}{3}+\sigma_3 \quad (10)$$

$$q_i=\frac{E_i}{1+\nu_i}\cdot(\varepsilon_{1i}-\varepsilon_{3i})=E_i\cdot\varepsilon_{1i} \quad (11)$$

Thus, the changes in the modulus of elasticity and the Poisson's ratio of sand during the static triaxial compression test are determined from Equations (12) and (5).

$$E_i=\frac{\sigma_{1i}-\sigma_3}{\varepsilon_{1i}}=\frac{q_i}{\varepsilon_{1i}} \quad (12)$$

To observe the damage in the modulus of elasticity and the change in the Poisson ratio during the behavior of drained sand at monotonic loading, we can initially use the experimental results of different samples of Toyoura sand at confining pressures similar to the characteristics

of Figure 1 [9]. In this Figure, e_0 is the initial void ratio and p'_0 to the initial mean effective stress, σ_3.

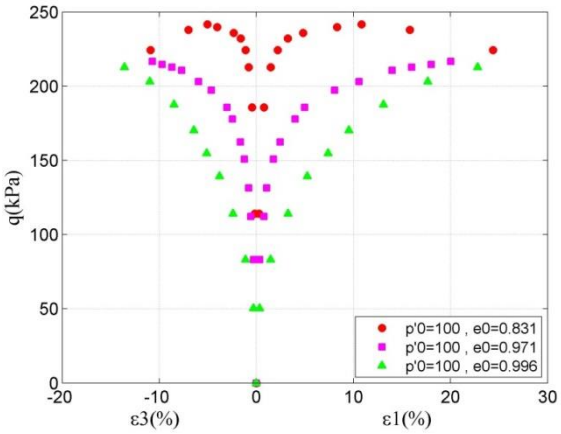

Fig. 1. Behavioral curves in drained triaxial compression tests on Toyoura sand samples [9]

For Toyoura sand samples, damages in the modulus of elasticity can be calculated using Equation (12) and plotted against axial strain, as shown in Figure 2.

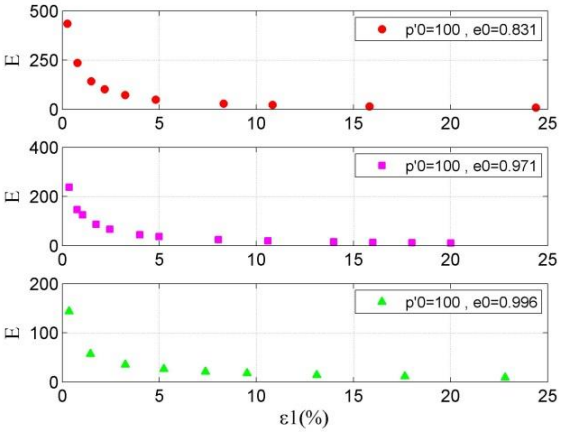

Fig. 2. The trend of modulus of elasticity damages with increasing axial strain in drained triaxial compression tests on Toyoyra sand samples

The graphical results of Figure 2 for the sand samples show that the modulus of elasticity is damaged and decreases during loading with increasing axial strain.
For Toyoura sand samples, changes in the Poisson's ratio can be calculated using Equation (5) and plotted against axial strain, as shown in Figure 3.
Thus, damages in the modulus of elasticity and changes in the Poisson ratio during the experiment caused nonlinear sand behavior, which is the criterion for numerical analysis of this research.

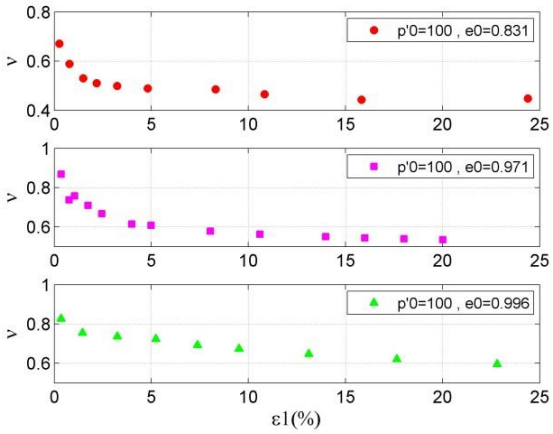

Fig. 3. The trend of changes in the Poisson ratio with increasing axial strain in drained triaxial compression tests on Toyoura sand samples

2.2. Defining numerical relationships of damage and changes

Based on the study conducted in this research, defining the *N* parameter according to Equation (13) can be used.

$$N = log(\frac{q}{\varepsilon_1}) = log(E) \quad for \quad \varepsilon_1 > 0 \tag{13}$$

This initiative makes it possible to define the resulting experimental curve with a three-coefficient mathematical function according to Equation (14) by calculating and plotting the *N* versus ε_1 variations for the experimental samples.

$$f(\varepsilon_1) = A \cdot (\varepsilon_1)^B + C \tag{14}$$

In this regard, *f* is a function that can express the effect of axial strain on damage in the modulus of elasticity. Numerical coefficients *A*, *B*, and *C* are also obtained based on the numerical function f on the experimental variations *N*.
Using Equation 14 in Equation 13, we can conclude Equations 15 and 16.

$$N = log(\frac{q}{\varepsilon_1}) = log(E) = f(\varepsilon_1) \quad \Rightarrow$$

$$q = \varepsilon_1 \cdot 10^f \tag{15}$$

$$E = 10^f \tag{16}$$

Numerical Equation (16) defines the trend of changes in the modulus of elasticity *E* in each loading increment *i* in terms of the principal strain ε_1.
Following the studies conducted in this research, it is better to start the Poisson's ratio changes during the experiment by defining the *M* parameter according to Equation (17).

$$M = log(2 - \varepsilon_3) \tag{17}$$

By calculating and plotting the changes of *M* versus ε_1 for the experimental samples, the resulting experimental curve can be defined by a four-coefficient mathematical function according to Equation (18).

$$g(\varepsilon_1) = a \cdot exp(b \cdot \varepsilon_1) + c \cdot exp(d \cdot \varepsilon_1) \tag{18}$$

In this regard, g is a function that can represent the effect of axial strain on the Poisson ratio. Numerical coefficients

a, *b*, *c*, and d are also obtained based on the mathematical function *g* on the experimental variations *M*.
Thus, using Equation (5) in Equation (17) and applying Equation (18), we can conclude Equation (19).

$$M = log(2 + \nu \cdot \varepsilon_1) = g(\varepsilon_1) \quad \Rightarrow$$

$$\nu = \frac{1}{\varepsilon_1} \cdot (10^g - 2) \tag{19}$$

Numerical Equation (19) defines the rate of change of the Poisson ratio in each loading increment *i* in terms of principal strain.

2.3. Numerical analysis process

In summary, the numerical analysis process considered in this research can be expressed as follows:

- Based on the experimental results of monotonic loading on the sand sample, *N* and *M* parameters are calculated according to Equations (13) and (17). Their variations against axial strain ε_1 are plotted.
- From Equation (14) on the plotting curve obtained from Equation (13), the numerical coefficients *A*, *B*, and *C* are calculated, and the function *f* is defined.
- From Equation (18) on the plotting curve obtained from Equation (17), the numerical coefficients *a*, *b*, *c*, and *d* are calculated, and the function *g* is defined.
- By defining the numerical functions *f* and *g*, the modulus of elasticity *E* and the Poisson's ratio ν in each loading increment *i* are determined from Equations (16) and (19).
- Lateral strain ε_3 and volumetric strain ε_v in loading increment *i* are calculated from equations (5) and (9).
- The mean and shear stress *p* and *q* are determined from equations (10) and (11).

The recent analytical process algorithm is shown in the flowchart of Figure 4.

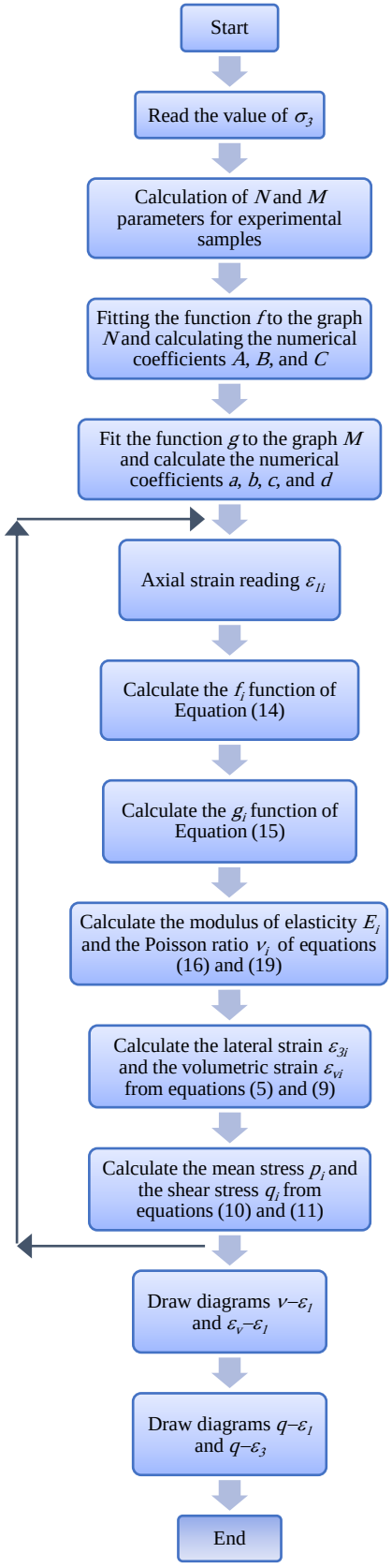

Fig. 4. Flowchart of numerical analysis

3. Examining the results of numerical analysis

In this section, the validity of the proposed numerical analysis is examined. For this purpose, calibration and comparison with related experimental results are used.

3.1. Calibration and comparison of numerical analysis results with a drained triaxial compression test on Toyoura sand

Initially, the drained triaxial compression test results of Toyoura sand samples at confining pressure of 100 kPa are used [9]. The experimental behavior of the recent samples is converted to numerical behavior and compared with each other, based on the proposed algorithm of Figure 4, as follows.
Parameter *N* is calculated from experimental results, and according to Equation (13), its changes against the axial strain ε_1 are plotted. Then, according to Figure 5, from the fit of the numerical relation 14 on the resulting curves, the numerical coefficients *A*, *B* and *C* are determined and are inserted in Table 1 to define the numerical function *f*.

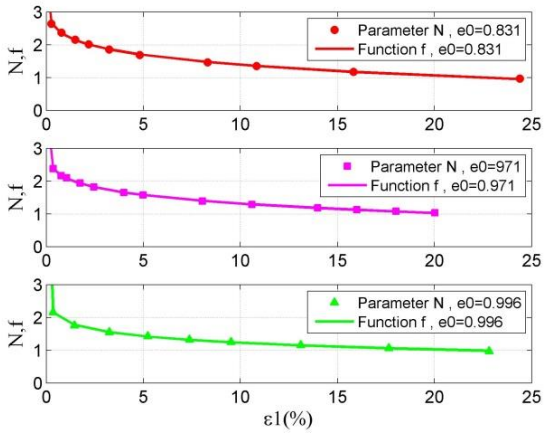

Fig. 5. Plotting the changes of parameter N against axial strain ε_1 and fitting the function f on it in the drained triaxial compression test on Toyoura sand samples (p'_0=100 kPa)

Table 1
The values of the coefficients of the function f for Toyoura sand samples (p'_0=100 kPa)

□□(kPa)	e_0	A	B	C
100	0.831	-2.047	0.1557	4.319
100	0.971	-2.255	0.1294	4.351
100	0.996	-6.978	0.3845	8.852

- The M parameter is determined from the experimental results according to Equation (17), and its changes against the ε_1 axial strain are plotted. Then, according to Figure 6, from the fit of the numerical relation 18 on the resulting curves, the numerical coefficients a, b, c, and d are calculated and inserted in Table 2 to define the numerical function g.

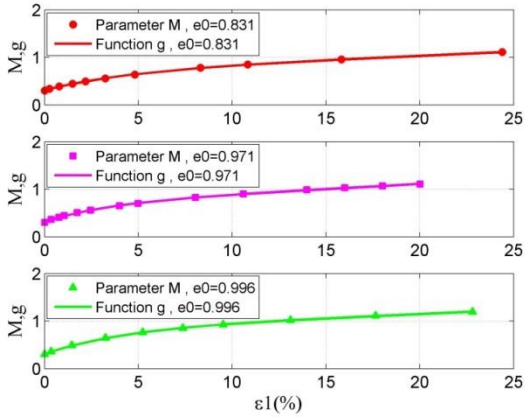

Fig. 6. Plotting the changes of parameter M against axial strain ε_1 and fitting function g on it in the drained triaxial compression test on Toyoura sand samples (p'_0=100 kPa)

Table 2
The values of the coefficients of the function g for Toyoura sand samples (p'_0=100 kPa)

σ_3 (kPa)	e_0	a	b	c	d
100	0.831	0.7595	0.01575	-0.4498	-0.1965
100	0.971	0.7552	0.01946	-0.4390	-0.2570
100	0.996	0.8650	0.01438	-0.5564	-0.2282

- The modulus of elasticity E is determined from Equation (16), and its changes against the axial strain ε_1 are plotted and compared with the experimental results as shown in Figure 7.

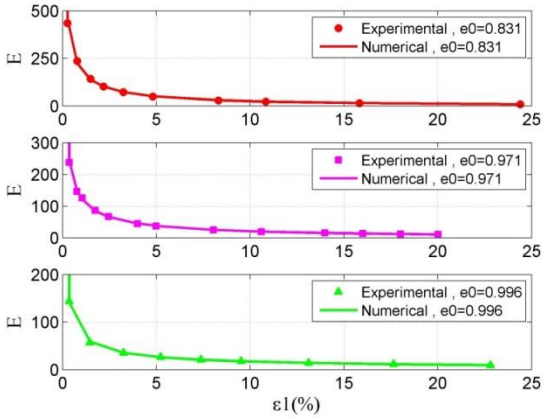

Fig. 7. Diagram of changes E–ε_1 for Toyoura sand samples (p'_0=100 kPa) and comparison of numerical analysis results with the drained triaxial compression test

- The Poisson ratio ν is determined from Equation (19), and its variations against the axial strain ε_1 are plotted and compared with the experimental results as shown in Figure 8.

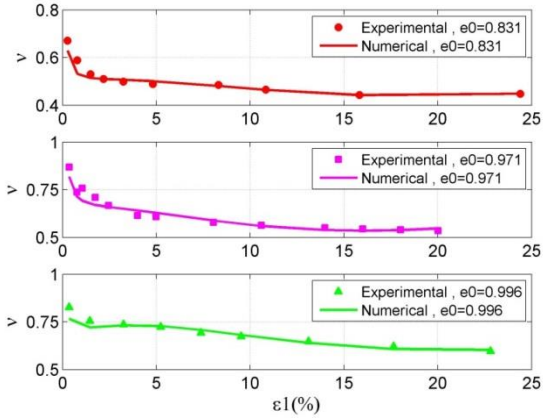

Fig. 8. Diagram of ν–ε_1 changes for Toyoura sand samples (p'_0=100 kPa) and comparison of numerical analysis results with the drained triaxial compression test

- Lateral strain ε_3 and volumetric strain ε_v are calculated from equations (5) and (9). The changes in volumetric strain ε_v versus axial strain ε_1 are plotted and, as shown in Figure 9, offer a good agreement with the experimental results.

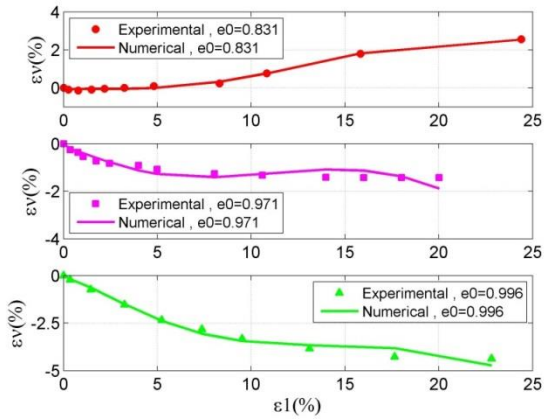

Fig. 9. Diagram of changes ε_v–ε_1 for Toyoura sand samples (p'_0=100 kPa) and comparison of numerical analysis results with the drained triaxial compression test

- The mean and shear stress p and q are determined from equations (10) and (11). The shear stress changes q against the axial strain ε_1 are plotted and, according to Figure 10, show a good agreement with the experimental results.

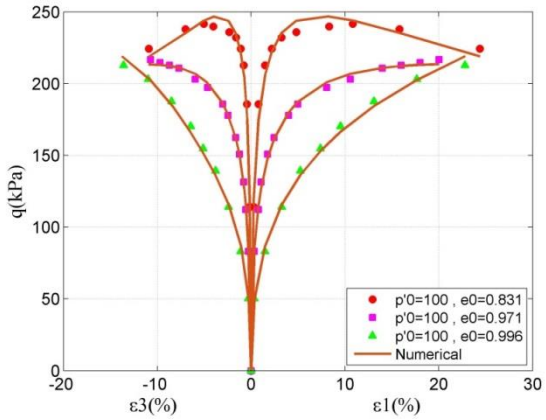

Fig. 10. Diagram of changes q–ε_1 for Toyoura sand samples (p'_0=100 kPa) and comparison of numerical analysis results with the drained triaxial compression test

In another review, the drained triaxial compression test results of Toyoura sand samples at confining pressure of 500 kPa are used [9]. For this purpose, the numerical analysis parameters for these samples are determined similar to the previous case, and the obtained results are compared with the experimental results. The coefficients obtained in Tables 3 and 4 and the comparative plotting results are presented in Figures 11 to 16.

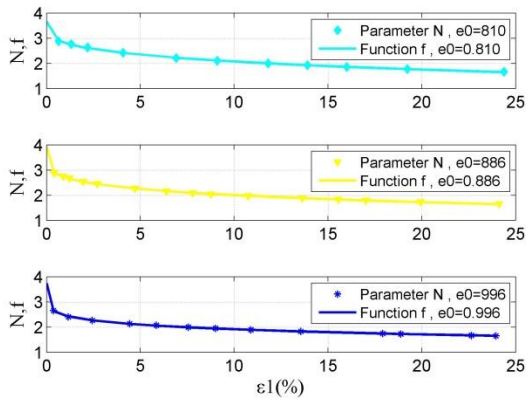

Fig. 11. Plotting the changes of parameter N against axial strain ε_1 and fitting the function f on it in the drained triaxial compression test on Toyoura sand samples (p'_0=500 kPa)

Table 3
The values of the coefficients of the function f for Toyoura sand samples (p'_0=500 kPa)

σ_3 (kPa)	e_0	A	B	C
500	0.810	-0.8457	0.2696	3.3648
500	0.886	-1.2180	01969	3.9210
500	0.960	-1.2860	0.1527	3.7420

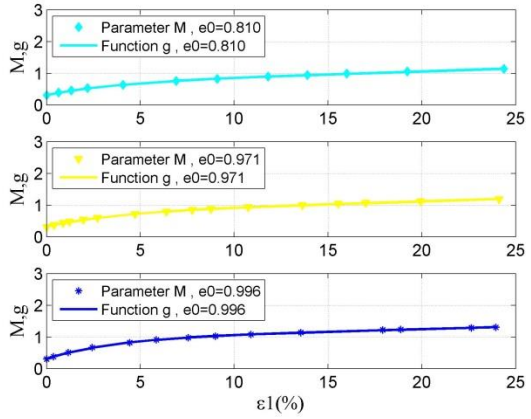

Fig. 12. Plotting the changes of parameter M against axial strain ε_1 and fitting function g on it in the drained triaxial compression test on Toyoura sand samples (p'_0=500 kPa)

Table 4
The values of the coefficients of the function g for Toyoura sand samples (p'_0=500 kPa)

σ_3 (kPa)	e_0	a	b	c	d
500	0.810	0.7488	0.01736	-0.4366	-0.2406
500	0.886	0.8210	0.01553	-0.5022	-0.2385
500	0.960	0.9726	0.01249	-0.6655	-0.2705

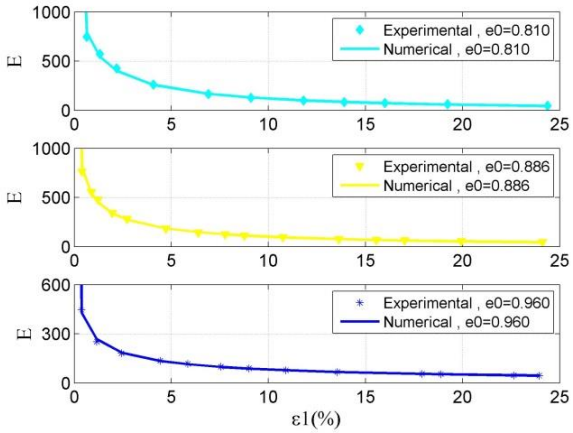

Fig. 13. Diagram of changes E–ε_1 for Toyoura sand samples (p'_0=500 kPa) and comparison of numerical analysis results with the drained triaxial compression test

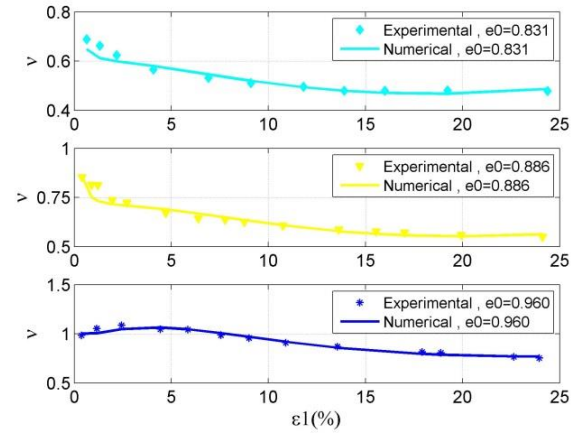

Fig. 14. Diagram of ν–ε_1 changes for Toyoura sand samples (p'_0=500 kPa) and comparison of numerical analysis results with the drained triaxial compression test

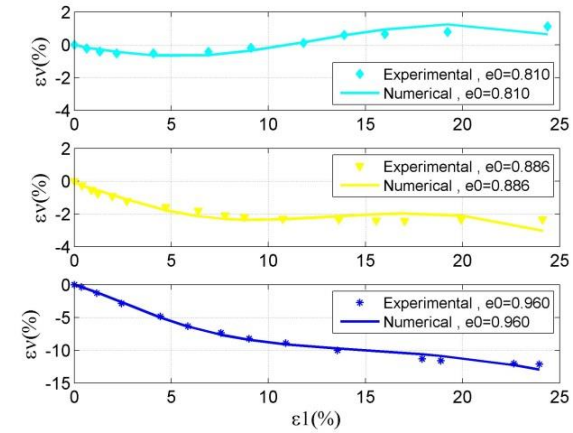

Fig. 15. Diagram of changes ε_v–ε_1 for Toyoura sand samples (p'_0=500 kPa) and comparison of numerical analysis results with the drained triaxial compression test

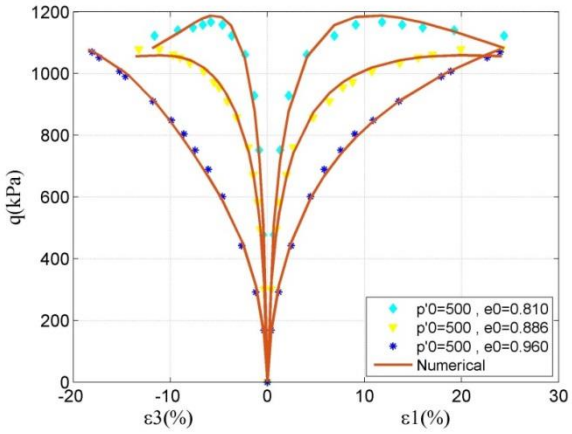

Fig. 16. Diagram of changes q–ε_1 for Toyoura sand samples (p'_0=500 kPa) and comparison of numerical analysis results with the drained triaxial compression test

According to the comparison of recent results, the conversion of the experimental behavior of Toyoura sand samples into numerical behavior can be considered appropriate and acceptable.

3.2. Calibration and comparison of numerical analysis results with a drained triaxial compression test on Nevada sand

Initially, the drained triaxial compression test results of Nevada sand samples at a relative density of 40% are used [35]. According to the available experimental information, the coefficients obtained in Tables 5 6 and the calibration and graphic comparison results are presented in Figures 17 to 22.

Table 5
The values of the coefficients of the function f for Nevada sand samples (D_r=40%)

σ_3 (kPa)	D_r(%)	A	B	C
40	40	-5.358	0.07074	7.064
80	40	-3.240	011140	5.191
160	40	-3.453	0.10640	5.744

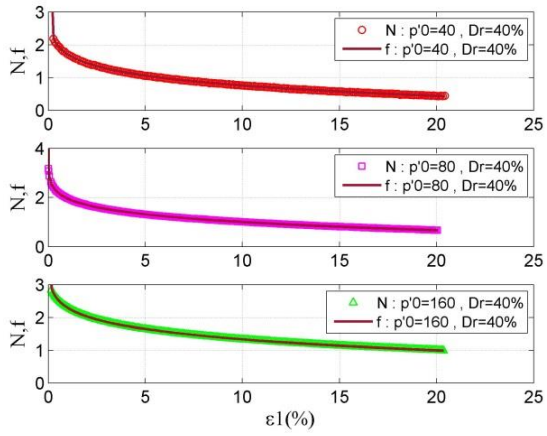

Fig. 17. Plotting the changes of parameter N against axial strain ε_1 and fitting the function f on it in the drained triaxial compression test on Nevada sand samples (D_r=40%)

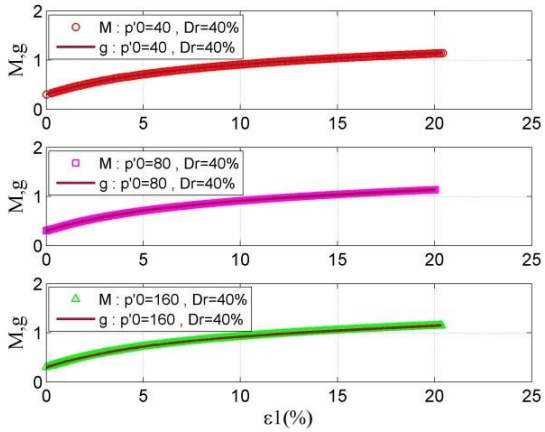

Fig. 18. Plotting the changes of parameter M against axial strain ε_1 and fitting function g on it in the drained triaxial compression test on Nevada sand samples (D_r=40%)

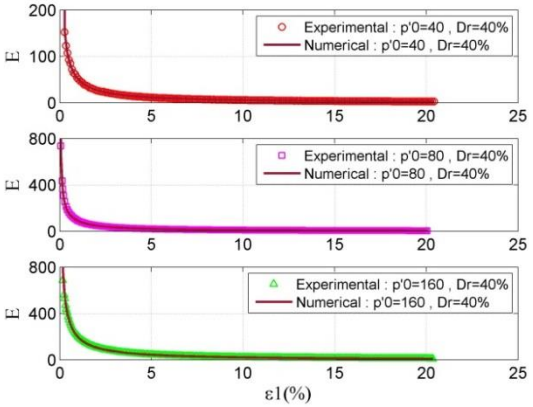

Fig. 19. Diagram of changes $E-\varepsilon_1$ for Nevada sand samples (D_r=40%) and comparison of numerical analysis results with the drained triaxial compression test

Table 6
The values of the coefficients of the function g for Nevada sand samples (D_r=40%)

σ_3 (kPa)	D_r(%)	a	b	c	d
40	40	0.8617	0.01446	-0.559	-0.1914
80	40	0.8571	0.01472	-0.554	-0.1907
160	40	0.8625	0.01460	-0.564	-0.1990

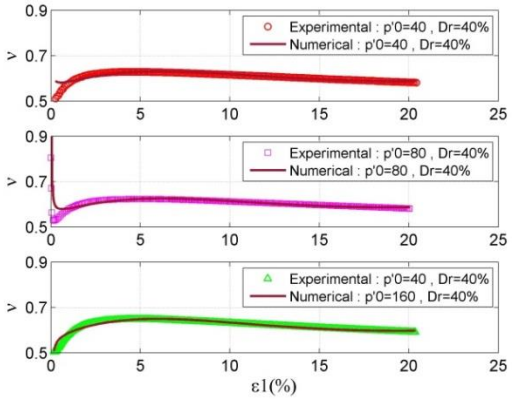

Fig. 20. Diagram of $\nu-\varepsilon_1$ changes for Nevada sand samples (D_r=40%) and comparison of numerical analysis results with the drained triaxial compression test

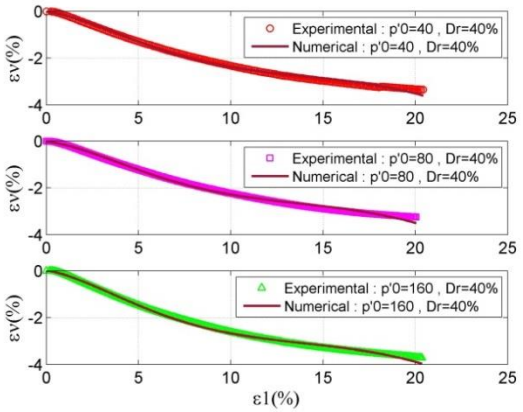

Fig. 21. Diagram of changes $\varepsilon_v-\varepsilon_1$ for Nvada sand samples (D_r=40%) and comparison of numerical analysis results with the drained triaxial compression test

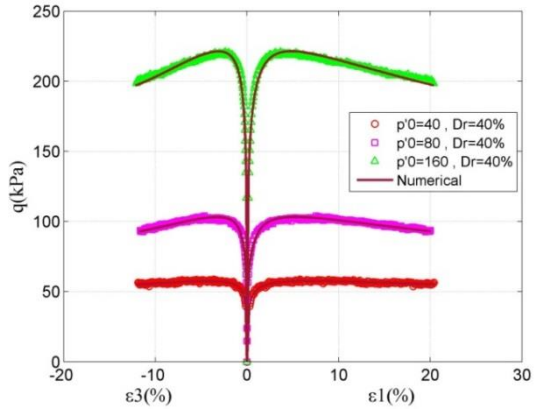

Fig. 22. Diagram of changes $q-\varepsilon_1$ for Nevada sand samples (D_r=40%) and comparison of numerical analysis results with the drained triaxial compression test

In another review, the drained triaxial compression test results of Nevada sand samples at a relative density of 60% are used [35]. For this purpose, the characteristics of numerical analysis for these samples are determined similar to the previous case, and the obtained results are compared with the experimental results. The coefficients obtained in Tables 7 and 8 and the comparative graphic results are presented in Figures 23 to 28.

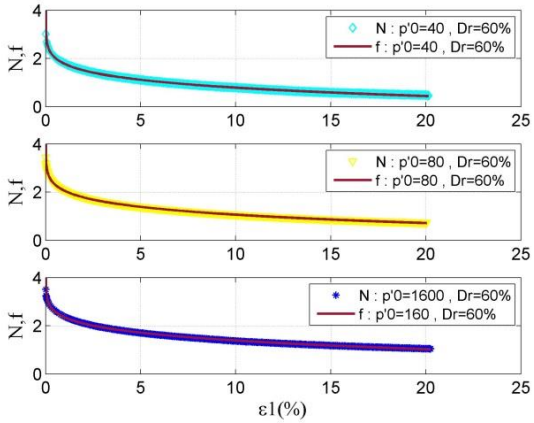

Fig. 23. Plotting the changes of parameter N against axial strain ε_1 and fitting the function f on it in the drained triaxial compression test on Nevada sand samples (D_r=60%)

Table 7
The values of the coefficients of the function *f* for Nevada sand samples (D_r=60%)

σ_3 (kPa)	D_r(%)	A	B	C
40	60	-3.357	0.1117	5.132
80	60	-3.580	0.1058	5.632
160	60	-2.381	0.1474	4.732

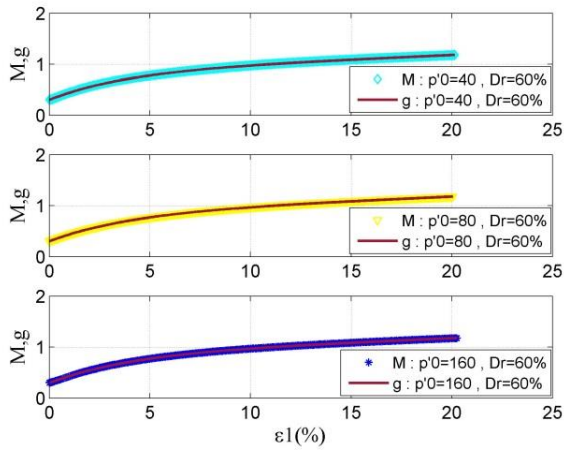

Fig. 24. Plotting the changes of parameter *M* against axial strain ε_1 and fitting function *g* on it in the drained triaxial compression test on Nevada sand samples (D_r=60%)

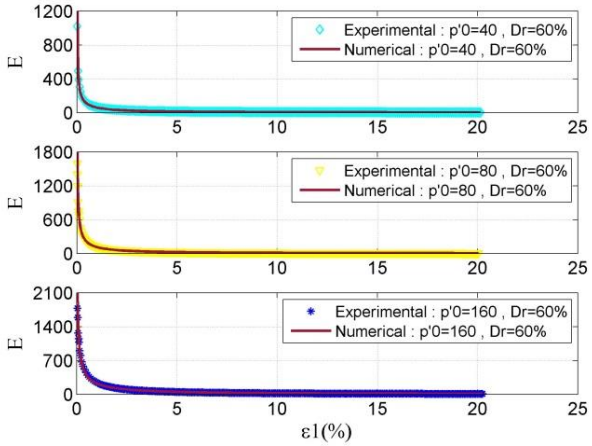

Fig. 25. Diagram of changes E–ε_1 for Nevada sand samples (D_r=60%) and comparison of numerical analysis results with the drained triaxial compression test

Table 8
The values of the coefficients of the function *g* for Nevada sand samples (D_r=60%)

σ_3 (kPa)	D_r(%)	a	b	c	d
40	60	0.8915	0.01425	-0.5908	-0.2405
80	60	0.8922	0.01417	-0.5898	-0.2284
160	60	0.8984	0.01368	-0.6033	-0.2314

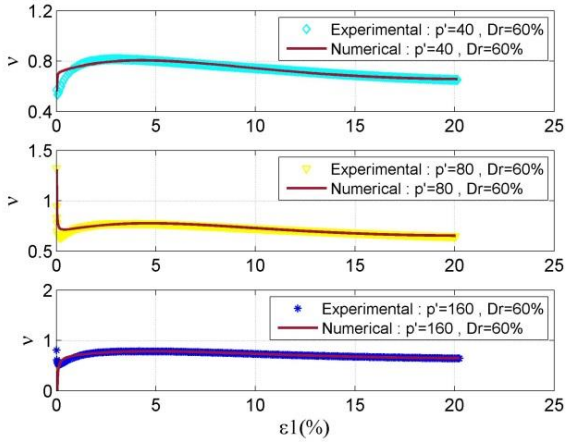

Fig. 26. Diagram of ν–ε_1 changes for Nevada sand samples (D_r=60%) and comparison of numerical analysis results with the drained triaxial compression test

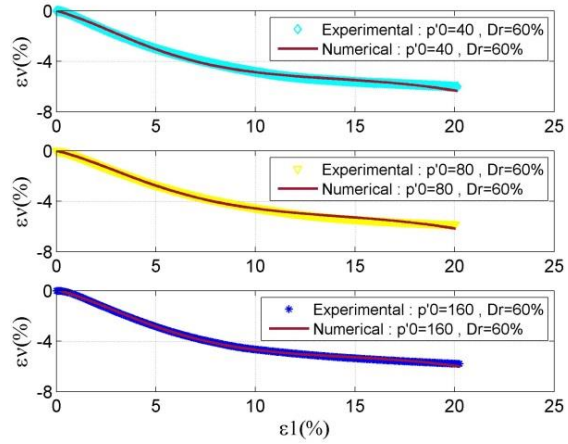

Fig. 27. Diagram of changes ε_v–ε_1 for Nvada sand samples (D_r=60%) and comparison of numerical analysis results with the drained triaxial compression test

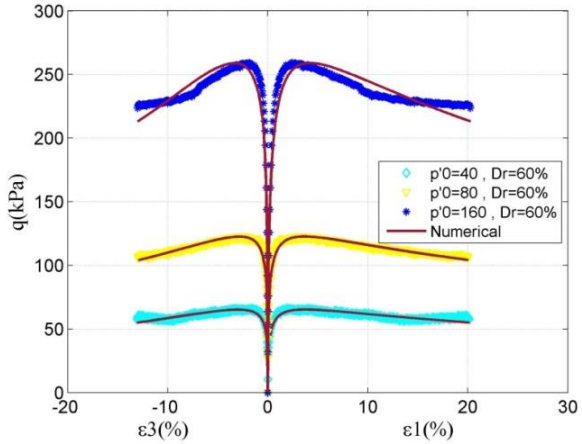

Fig. 28. Diagram of changes q–ε_1 for Nevada sand samples (D_r=60%) and comparison of numerical analysis results with the drained triaxial compression test

According to the comparison of recent results, the conversion of the experimental behavior of Nevada sand samples into numerical behavior can be considered appropriate and acceptable.

3.3. Calibration and comparison of numerical analysis results with a drained triaxial compression test on Houston sand

This section uses the drained triaxial compression test results of Houston sand samples [20]. Similar to the previous cases, the coefficients obtained in Tables 9 and 10 and the calibration and graphical comparison are presented in Figures 29 to 34.

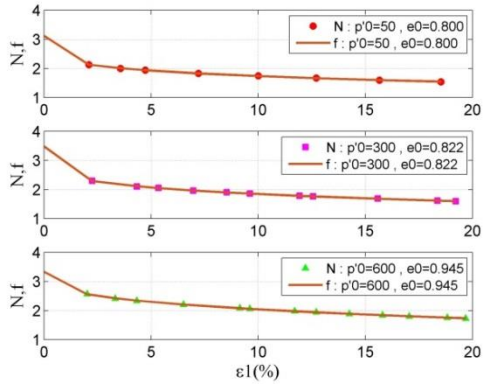

Fig. 29. Plotting the changes of parameter N against axial strain ε_1 and fitting the function f on it in the drained triaxial compression test on Houston sand samples

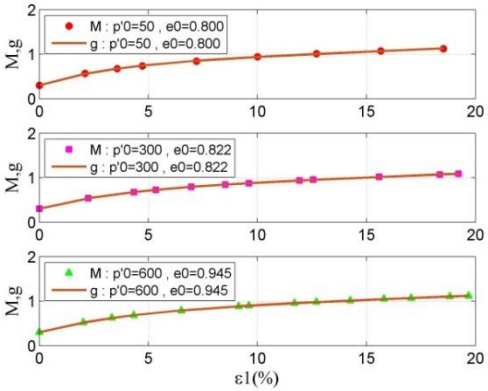

Fig. 30. Plotting the changes of parameter M against axial strain ε_1 and fitting function g on it in the drained triaxial compression test on Houston sand samples

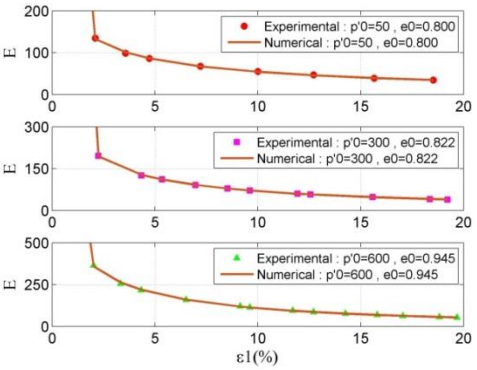

Fig. 31. Diagram of changes E–ε_1 for Houston sand samples and comparison of numerical analysis results with the drained triaxial compression test

Table 9
The values of the coefficients of the function f for Houston sand samples

σ_3 (kPa)	e_0	A	B	C
50	0.800	-0.8472	0.2117	3.114
300	0.822	-1.0030	0.2128	3.479
600	0.945	-0.6210	0.3175	3.330

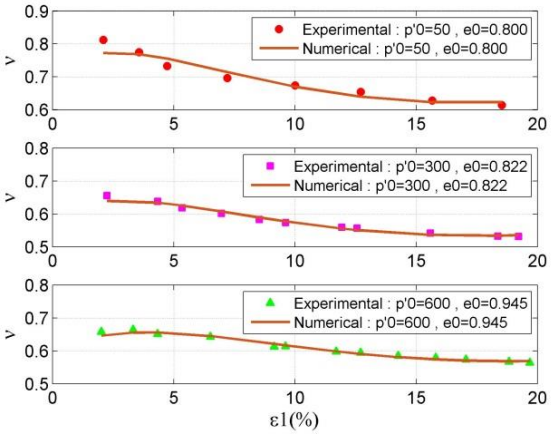

Fig.32. Diagram of ν–ε_1 changes for Houston sand samples and comparison of numerical analysis results with the drained triaxial compression test

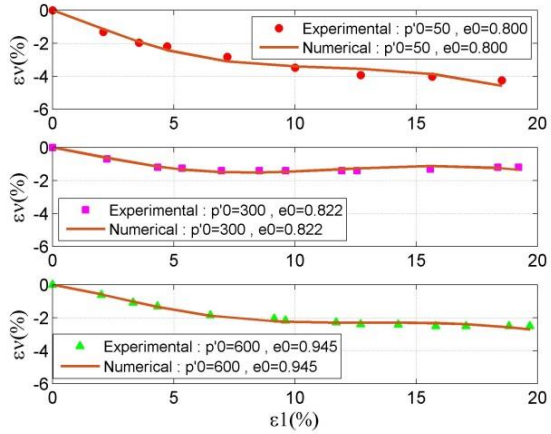

Fig.33. Diagram of changes ε_v–ε_1 for Houston sand samples and comparison of numerical analysis results with the drained triaxial compression test

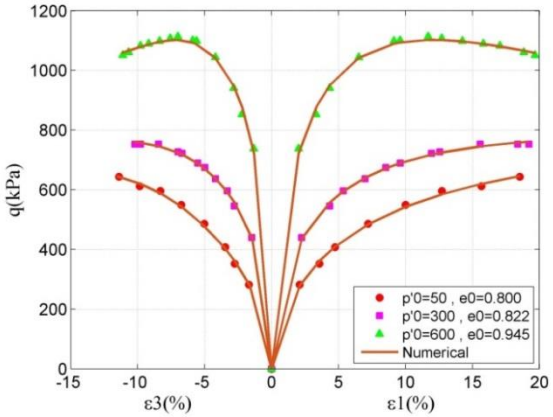

Fig.34. Diagram of changes q–ε_1 for Houston sand samples and comparison of numerical analysis results with the drained triaxial compression test

Table 10
The values of the coefficients of the function g for Houston sand samples

□□(kPa)	e_0	*a*	*b*	*c*	*d*
50	0.800	0.8088	0.01829	-0.5044	-0.2778
300	0.822	0.7779	0.01773	-0.4751	-0.2461
600	0.945	0.8229	0.01597	-0.5202	-0.2243

The conversion of the experimental behavior of Houston sand samples to numerical behavior is also considered very appropriate.

4. **Conclusion**

This paper investigated the experimental behavior of different sand samples in monotonic loading and drained conditions, and hypo-elastic was assumed. Based on the observation of damages in the modulus of elasticity and changes in the Poisson ratio during loading, a numerical and straightforward analytical method was presented to define the linear-nonlinear behavior of sand. The calibration of this method was evaluated using the related experimental results on different sand samples. The results of studies, calculations, and comparisons in this research show that designing and achieving this numerical method is valuable. Because it has neither the complexities of micro behavioral models nor the problems of macro behavioral models, it is presented as a simple numerical behavioral analysis. In a general summary, the salient features of this method can be expressed as follows:

1. This numerical method saves time and money with convenient and straightforward computational logic.
2. The function *f* has three coefficients to calculate the damages in the modulus of elasticity, and its calibration is simple with the changes of the experimental parameter *N*.
3. The mathematical relation *g* has four coefficients to calculate the changes in the Poisson ratio, and its calibration with the changes of the experimental parameter *M* requires accuracy.
4. The proposed numerical analysis can present the softening behavior of sand types. This is not seen in many models or at a high computational cost.
5. Simple numerical analysis process this method is admirable compared to dough models.
6. The proposed numerical method can define the non-isotropic behavior of sand in pressure, tension and shear and provide more value in multi-laminate models.

It is noteworthy that this numerical method is being completed for other loading conditions and modes and placed in multi-laminate models.

References

1. Ishihara, Kenji, Fumio Tatsuoka, and Susumu Yasuda. "Undrained deformation and liquefaction of sand under cyclic stresses." Soils and foundations 15.1 (1975): 29-44.
2. Li, Yanlong, et al. "A study of the overtopping breach of a sand-gravel embankment dam using experimental models." *Engineering Failure Analysis* 124 (2021): 105360.
3. Zienkiewicz, O. C., and Z. Mroz. "Generalized plasticity formulation and applications to geomechanics." Mechanics of engineering materials 44.3 (1984): 655-680.
4. Pastor, M., O. C. Zienkiewicz, and K. H. Leung. "Simple model for transient soil loading in earthquake analysis. II. Non-associative models for sands." International Journal for Numerical and Analytical Methods in Geomechanics 9.5 (1985): 477-498.
5. Pastor, M., O. C. Zienkiewicz, and A. H. C. Chan. "Generalized plasticity and the modelling of soil behaviour." International Journal for Numerical and Analytical Methods in Geomechanics 14.3 (1990): 151-190.
6. Verdugo, Ramon, and Kenji Ishihara. "The steady state of sandy soils." Soils and foundations 36.2 (1996): 81-91.
7. Dafalias, Yannis F., and Majid T. Manzari. "Simple plasticity sand model accounting for fabric change effects." Journal of Engineering mechanics 130.6 (2004): 622-634.
8. Ling, Hoe I., and Songtao Yang. "Unified sand model based on the critical state and generalized plasticity." Journal of Engineering Mechanics 132.12 (2006): 1380-1391.
9. Manzanal, Diego, José Antonio Fernández Merodo, and Manuel Pastor. "Generalized plasticity state parameter-based model for saturated and unsaturated soils. Part 1: Saturated state." International Journal for Numerical and Analytical Methods in Geomechanics 35.12 (2011): 1347-1362.
10. Sadrnejad, S. A., and G. N. Pande. "A multilaminate model for sands." Proc. Int. Symp. Num. Models in Geomech.(NUMOG III). 1989.
11. Sadrnejad, S. A. "Multilaminate elastoplastic model for granular media." International Journal of Engineering 5.1&2 (1992): 11.
12. Sadrnejad, S. A. "A general multi-plane model for post-liquefaction of sand." Iranian Journal of Science and Technology 31.B2 (2007): 123.
13. Sadrnejad, Seyed Amirodin, and Hamid Karimpour. "Drained and undrained sand behaviour by multilaminate bounding surface model." (2011): 111-125.
14. Daouadji, Ali, et al. "Experimental and numerical investigation of diffuse instability in granular materials using a microstructural model under various loading paths." Géotechnique 63.5 (2013): 368-381.
15. Ghafghazi, M., D. A. Shuttle, and J. T. DeJong. "Particle breakage and the critical state of sand." Soils and Foundations 54.3 (2014): 451-461.
16. Fang, H. L., H. Zheng, and J. Zheng. "Micromechanics-based multimechanism bounding surface model for sands." International Journal of Plasticity 90 (2017): 242-266.
17. Loukidis, D., and R. Salgado. "Modeling sand response using two-surface plasticity." *Computers and Geotechnics* 36.1-2 (2009): 166-186.
18. Jin, Yinfu, et al. "Unified modeling of the monotonic and cyclic behaviors of sand and clay." Acta Mechanica Solida Sinica 28.2 (2015): 111-132.
19. Woo, Sang Inn, and Rodrigo Salgado. "Bounding surface modeling of sand with consideration of fabric and its evolution during monotonic shearing." International Journal of Solids and Structures 63 (2015): 277-288.
20. Sun, Yifei, and Yang Xiao. "Fractional order plasticity model for granular soils subjected to monotonic triaxial compression." International Journal of Solids and Structures 118 (2017): 224-234.
21. Heidarzadeh, Heisam, and Mohammad Oliaei. "Development of a generalized model using a new plastic modulus based on bounding surface plasticity." *Acta Geotechnica* 13.4 (2018): 925-941.
22. Yang, Yanxin, and Edward Kavazanjian Jr. "Numerical evaluation of liquefaction-induced lateral spreading with an

advanced plasticity model for liquefiable sand." *Soil Dynamics and Earthquake Engineering* 149 (2021): 106871.
23. Wang, Zhiliang, and Fenggang Ma. "Bounding surface plasticity model for liquefaction of sand with various densities and initial stress conditions." *Soil Dynamics and Earthquake Engineering* 127 (2019): 105843.
24. Zhang, Fuguang, et al. "DEM analysis of cyclic liquefaction behaviour of cemented sand." *Computers and Geotechnics* 142 (2022): 104572.
25. Fang, Qin, et al. "Mesoscopic investigation of the sand particulate system subjected to intense dynamic loadings." *International Journal of Impact Engineering* 89 (2016): 62-71.
26. Peyman Farzad, and Seyed A. Sadrnejad. "Liquefied Residual Strength of Undrained Sand upon A Parametric Approach to Hypo-elastic Model" Numerical Methods in Civil Engineering (2017).
27. Sadrnejad, S. A., and Sh Shakeri. "Fabric assessment of damaged anisotropic geo-materials using the multi-laminate model." International Journal of Rock Mechanics and Mining Sciences 91 (2017): 90-103.
28. Sadrnejad, S. A., and Sh Shakeri. "Multi-laminate non-coaxial modelling of anisotropic sand behavior through damage formulation." Computers and Geotechnics 88 (2017): 18-31.
29. Zhang, Jinhua, Yadong Zhang, and Qin Fang. "Numerical simulation of shock wave propagation in dry sand based on a 3D mesoscopic model." *International Journal of Impact Engineering* 117 (2018): 102-112.
30. Dashti, Hadi, Seyed Amirodin Sadrnejad, and Navid Ganjian. "A novel semi-micro multilaminate elasto-plastic model for the liquefaction of sand." *Soil Dynamics and Earthquake Engineering* 124 (2019): 121-135.
31. Li, Haoyang, et al. "Three-dimensional mesoscopic investigation on equation of state for dry sand under shock compression." *International Journal of Impact Engineering* 160 (2022): 104060.
32. Evangelista Jr, Francisco, and José Fabiano Araújo Moreira. "A novel continuum damage model to simulate quasi-brittle failure in mode I and mixed-mode conditions using a continuous or a continuous-discontinuous strategy." *Theoretical and Applied Fracture Mechanics* 109 (2020): 102745.
33. Li, Ruidong, et al. "A systematic framework for DEM study of realistic gravel-sand mixture from particle recognition to macro-and micro-mechanical analysis." *Transportation Geotechnics* (2021): 100693.
34. Peyman, Farzad, and Seyed A. Sadrnejad. "Analysis of concrete crack growth based on micro-plane model." Structural Concrete 19.3 (2018): 930-945.
35. Arulmoli, K., Muraleetharan, K. K., Hosain, M. M., & Fruth, L. S. (1992). VELACS laboratory testing program, soil data report. *The Earth Technology Corporation, Irvine, California, Report to the National Science Foundation, Washington DC*.